

Control of the Probe-Sample Interaction Force at the Piconewton Scale by a Magnetic Microprobe in Aqueous Solutions

Ta-Min Meng  and Chia-Hsiang Menq 

Abstract—This article describes the design and implementation of a control system that controls the probe-sample interaction force at the piconewton scale by manipulating a magnetic microprobe in aqueous solutions under a microscope. The control system has two functions, namely accurate force generation by magnetic flux control and precise control of the probe-sample interaction force. Magnetic flux control uses an improved six-input-six-output digital control law along with a disturbance estimator to achieve two control objectives. First, the magnetic flux at each pole tip of a previously developed hexapole electromagnetic actuator can be individually and precisely controlled at frequencies over 4 kHz, and the experimental results precisely followed the theoretical predictions based on the design. Second, together with the optimized flux allocation, the flux control system generates precise magnetic forces, making the six-input hexapole actuator behave like a decoupled three-axis force generator with a bandwidth of more than 4 kHz. Interaction force control compares the measured deformation of the sample with the expected deformation, updated in real time by a deformation predictor, to generate the magnetic force to control the interaction between the probe and the sample. Digital control laws, the estimator, and the predictor are all implemented using a high-speed Field Programmable Gate Array (FPGA) system. Experiments confirm that through mathematical modeling, digital control technology, high-speed electronics, and real-time computation, accurate three-dimensional force generation at the piconewton scale with high bandwidth and precise interaction force control with zero-mean random error, attributed to random thermal force and measurement noise, are achieved.

Index Terms—Electromagnetic actuation, interaction force control, magnetic flux control.

I. INTRODUCTION

ELCTROMAGNETIC actuators are widely used in a variety of applications, including magnetic levitation of

Manuscript received 22 November 2022; revised 24 March 2023; accepted 18 May 2023. Recommended by Technical Editor J. Schultz and Senior Editor Y. Li. This work was supported in part by the endowment fund for the Ralph W. Kurtz Chair in Mechanical Engineering at the Ohio State University. (*Corresponding author: Chia-Hsiang Menq.*)

The authors are with the Department of Mechanical and Aerospace Engineering, The Ohio State University, Columbus, OH 43210 USA (e-mail: meng.350@osu.edu; menq.1@osu.edu).

Color versions of one or more figures in this article are available at <https://doi.org/10.1109/TMECH.2023.3278730>.

Digital Object Identifier 10.1109/TMECH.2023.3278730

multiaxis motion devices [1], [2], propulsion of miniature swimming machines [3], [4], [5], multiaxis scanning probe technology [6], [7], and control of medical devices [8], [9], [10], [11], [12]. More recently, they have been used to enable untethered manipulation of microprobes in force spectroscopy [13], leading to advanced techniques employed in biomedical research. Specifically, magnetic tweezers have been developed to probe biological processes closely related to interaction forces ranging from subpiconewtons (pN) to tens of piconewtons scales [14], [15], [16], e.g., manipulating macromolecules [17], [18], [19], steering magnetic particles and microrobots [4], [5], [11], [12], [20], [21], [22], probing cell membranes [23], [24], and measuring intracellular properties [25].

To provide scanning probe functionality using magnetic tweezer technology, a hexapole electromagnetic actuator along with a visual servo control system was developed to enable 3-D magnetic actuation and stable trapping of a single magnetic microprobe in aqueous solutions [22]. A newer hexapole actuator has recently been developed to significantly improve its force generation capability [26]. It uses six pointed poles, each made of iron-steel rod and driven by separate coils. All coils and poles are magnetically connected by a yoke to enhance the generation of magnetic flux. Optimal current allocation associated with hexapole actuation [27] was devised to solve four problems in force generation, namely: redundancy; coupling; nonlinearity; and position-dependency. It was implemented in an FPGA system for real-time current allocation to enable current-based control of the probing system.

While current-based control enables stable magnetic trapping and visual servo control [26], [27], magnetic remanence and hysteresis could lead to uncertainties in magnetic flux generation. These uncertainties increase when greater forces need to be generated, leading to greater force errors, and reducing the performance of the actuator. In addition, quasi-static relationships in current-based force models ignore the dynamics of magnetic flux generation, which is important for advanced applications that require high-bandwidth precision force generation. Aiming at the problem of positioning error caused by residual magnetic remanence, Hall-sensor-based magnetic force modeling and optimal flux allocation were developed [28]. In addition, a magnetic flux control system was developed to solve the problems caused by hysteresis and increase the bandwidth of magnetic force generation [29].

This article describes the design and implementation of a control system that controls the magnetic field in the 3-D workspace of a previously developed hexapole actuator [28] to control the magnetic force exerted on a magnetic microprobe as well as the probe-sample interaction force at the piconewton scale. Section II briefly reviews the experimental setup that uses the hexapole actuator to apply a controllable 3-D magnetic force to a single magnetic microprobe in aqueous solutions [27], as well as the most relevant results for magnetic force modeling and inverse modeling [28].

The control of the magnetic field is achieved by controlling the magnetic fluxes at the six pole tips that enclose the 3-D workspace of the actuator. Magnetic flux control is an improved version of the previous implementation [29], wherein a six-input-six-output discrete model was calibrated and used to design and analyze the magnetic flux control. Two main limitations were, however, observed experimentally. First, the control performance did not match the design. It was necessary to significantly reduce the control gain of the design to achieve stability in the experiment [29]. Second, even with experimental tuning of the control gain, the closed-loop bandwidth achieved was limited to less than 1 kHz.

The design, theoretical performance analysis, and experimental validation of the improved six-input-six-output control law are presented in Section III. The improved control law has three components: feedback control law designed according to the six-input-six-output discrete model of the hexapole actuator; disturbance estimator and disturbance compensation; and prefilter designed to increase the bandwidth of the flux control. Experiments have shown that whereas the hexapole actuator has multipole coupling, uncertainties caused by magnetic remanence and hysteresis, and limited bandwidth, with the improved six-input-six-output flux control, the magnetic flux at each pole tip can be individually and precisely controlled at frequencies over 4 kHz without any experimental tuning. More importantly, the experimental results precisely followed the theoretical predictions based on the design. Moreover, together with the optimized flux allocation, the developed flux control system generates precise magnetic forces, making the six-input hexapole system behave like a decoupled three-axis force generator with a bandwidth of more than 4 kHz.

The design and experimental verification of force control are described in Section IV. Interaction force control has three components: the parameter estimator that estimates time-varying indentation gain and elastic force in real time; the deformation predictor that uses the estimated parameters to predict the expected deformation; and the motion stabilizer that stabilizes the probe with the expected sample deformation. The control system compares the measured sample deformation with the expected deformation, updated in real time using Kalman filtering, to generate magnetic forces to control probe-sample interactions, while using a feedback control law to achieve motion stabilization. Experiments confirm that accurate 3-D force generation at the piconewton scale with a bandwidth over 4 kHz has been achieved and that precise control of the interaction force of the microprobe with a living cell has been demonstrated. The functions of the control system form the basis for automatic probing

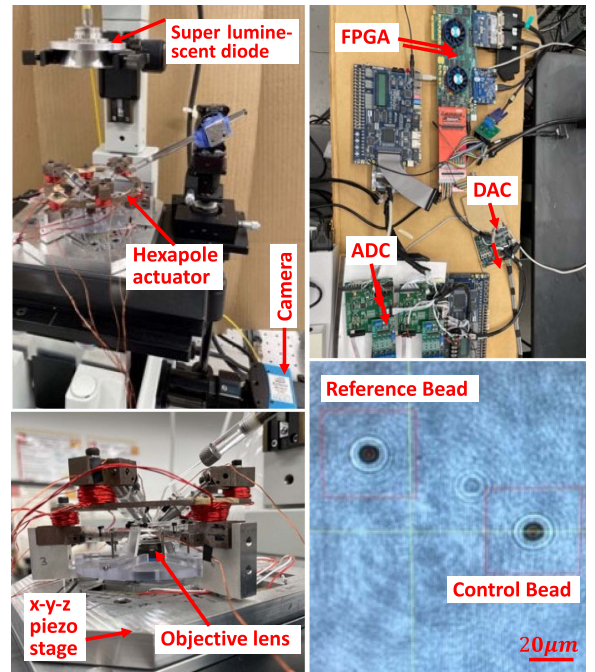


Fig. 1. Experimental setup for untethered manipulation of the magnetic probe in aqueous solutions (reproduced from Fig. 7 in [29]).

and controlled manipulation of active biological samples by the microprobe in aqueous solutions.

II. MANIPULATION OF MAGNETIC MICROPROBE

Fig. 1 shows a previously developed experimental setup that uses a hexapole electromagnetic actuator to apply controllable 3-D magnetic force for untethered manipulation of a single magnetic microprobe in aqueous solutions. The top left panel shows the hexapole actuator integrated with an inverted microscope (Olympus IX81) equipped with a CMOS camera (Mikrotron: MC3010) and an ultra-precise 3-D motion tracking system to form a 3-D visual servo control system [29]. The bottom left panel shows the hexapole system is assembled on an $x-y-z$ piezoelectric motion stage. The top right panel shows the electronics used for real-time image processing and digital control. The bottom right panel shows a typical real-time image.

The dynamics of the microscopic probe moving in aqueous solutions is governed by the Langevin equation at low Reynolds numbers [30]. When interacting with a sample, the motion of the probe is driven by the controllable magnetic force \mathbf{f}_m and affected by the probe-sample interaction force \mathbf{f}_I and random thermal force \mathbf{f}_T . By modeling the sample as an object having viscoelastic mechanical properties, the interaction force can be divided into two components, namely the elastic force and the damping force, i.e., $\mathbf{f}_I = \mathbf{f}_E + \mathbf{f}_D$. Therefore, the equation of motion is expressed as

$$\gamma \dot{\mathbf{p}}(t) = \mathbf{f}_m(\mathbf{p}(t), \mathbf{I}(t)) - \mathbf{f}_E(t) + \mathbf{f}_T(t), \quad (1)$$

where γ is the viscous damping coefficient matrix, \mathbf{p} the probe position, and \mathbf{I} the vector of the six input currents applied to the hexapole actuator.

When there is no probe-sample interaction, the goal of the manipulation is to stabilize the probe in aqueous solutions and steer the probe within the 3-D workspace [29], wherein \mathbf{f}_E vanishes and γ is the drag coefficient associated with the moving probe in aqueous solutions. When the microprobe is controlled to probe a sample, e.g., a live cell, \mathbf{f}_E varies nonlinearly with the deformation of the sample and γ is dominated by the nonlinear damping coefficient of the deformation process. The objective of control is to adjust the six input currents to generate the required magnetic force to stabilize the probe and control the interaction force of the probe with the sample.

A. Magnetic Gradient Force

Three pairs of pointed pole tips are symmetrically placed on three orthogonal axes, delineating the three axes of three-axis actuation, to concentrate the magnetic flux into the workspace, where the sample and the moving magnetic probe are placed [26]. The workspace is a polyhedron, whose size is determined by the distance between each individual pole tip and the center, denoted by ℓ . Although ℓ is adjustable, it is 500 micrometers for all experiments reported herein.

Two coordinate systems, i.e., the measurement coordinate system and the actuation coordinate system, are defined for measurement and actuation modeling, respectively. The z -axis of the measurement coordinate system is aligned with the optical axis of the microscope. A rotation matrix is defined to correlate the position coordinates of the probe between the two coordinate systems, i.e., ${}^M \mathbf{p} = {}^A \mathbf{R} {}^A \mathbf{p}$. The resulting gradient force is expressed as a flux-based force model with respect to the actuation coordinate system [28]

$${}^A \mathbf{f}_m ({}^A \mathbf{p}, \Phi) = g_\Phi \sum_{i=1}^6 \sum_{j=1}^6 \Phi_i \Phi_j \nabla \left(\frac{\mathbf{u}_i \cdot \mathbf{u}_j}{\hat{r}_i^2 \hat{r}_j^2} \right) \quad (2)$$

where $g_\Phi = [V\chi/(2\mu_0)]/[(4\pi)^2 \ell^5]$ denotes the force gain associated with the magnetic probe and the size of the workspace, V is the volume of and χ the magnetic susceptibility of the probe, and μ_0 is the vacuum magnetic permeability. It is seen that each of the three components of the 3-D gradient force is represented as a quadratic form in the six variables of the magnetic-flux vector, $\Phi = [\phi_1 \ \phi_2 \ \phi_3 \ \phi_4 \ \phi_5 \ \phi_6]^T$. It is worth noting that in the expression on the right side of (2) the position coordinates of the probe and the six pole tips, as well as the distance between them, are normalized with respect to the radius of the workspace ℓ , i.e., $\hat{\mathbf{p}} = \mathbf{p}/\ell$ and $\hat{r} = r/\ell$. Therefore, when referring to the normalized actuator coordinate system, the six magnetic tips are located at $\hat{x} = \pm 1$, $\hat{y} = \pm 1$, and $\hat{z} = \pm 1$, and $\nabla(\mathbf{u}_i \cdot \mathbf{u}_j / \hat{r}_i^2 \hat{r}_j^2)$ is dimensionless, depicting multipole coupling and position-dependence in hexapole actuation.

B. Optimal Flux Allocation

Assigning the correct value for the 6×1 controllable variables, Φ , to generate the desired 3×1 force, ${}^A \mathbf{f}_d$, is essential for the practical use of the hexapole actuator. In addition, the allocation of Φ is position-dependent and needs to be done in real time. A previously developed magnetic flux allocation method

[28] was implemented and used to control magnetic forces. It leads to optimal flux allocation to render effective 3-D force generation for real-time applications. The most relevant results are summarized below.

At a specified position of the probe and along a specified direction, $\Phi_{\text{opt}}(\varphi, \theta, {}^A \hat{\mathbf{p}})$ could be numerically determined by minimizing the Lagrange function using MATLAB optimization toolbox. Optimal solutions associated with predetermined positions ${}^A \hat{\mathbf{p}}_k$, covering the desired spatial range in the 3-D workspace, and along a set of selected discrete directions $\hat{\mathbf{r}}(\varphi_j, \theta_j)$, covering the entire 3-D orientation, were numerically determined. Least squares fitting was then employed to construct an analytical direction-dependent $6 \times 4 \times 4$ optimal flux-allocation matrix, $\mathbf{D}^{LS}(\varphi, \theta)$ [24], to serve as a kernel for optimal magnetic flux allocation

$$\hat{\Phi}_{\text{opt}}(\varphi, \theta, {}^A \hat{\mathbf{p}}) = \hat{\mathcal{P}}^T \mathbf{D}^{LS}(\varphi, \theta) \hat{\mathcal{P}} \quad (3)$$

where $\hat{\mathcal{P}} = [\hat{x}, \hat{y}, \hat{z}, 1]^T$ is the augmented position vector. Optimal flux allocation can then be determined by scaling

$$\Phi_{\text{opt}}({}^A \mathbf{f}_d, {}^A \hat{\mathbf{p}}) = \sqrt{\frac{f_d}{g_\phi}} \hat{\Phi}_{\text{opt}}(\varphi, \theta, {}^A \hat{\mathbf{p}}). \quad (4)$$

The magnetic flux is produced by the magnetomotive force, which is proportional to the input current, \mathbf{I} , and the turns of the coil, N_c . By Hopkinson's law in magnetic circuit analysis, the magnetic flux is quasi-statically related to the input current by $\Phi_I = (N_c/\mathcal{R}_a)\mathbf{K}_I \mathbf{I}$, where \mathcal{R}_a is the lumped magnetic reluctance and \mathbf{K}_I is the flux distribution matrix. This approach has been successfully applied to achieve stable visual-servo control of the magnetic probe in aqueous solutions [27]. However, it has three major limitations: lacking knowledge of accurate \mathcal{R}_a and \mathbf{K}_I ; suffering from uncertainty attributed to remanence and hysteresis in magnetic flux generation; and ignoring the dynamic of magnetic flux generation.

C. Measurement of Magnetic Flux

Direct measurement of magnetic flux is used to solve problems in current-based magnetic flux generation. The approach is to integrate six Hall sensors into the hexapole actuator. Due to the size of the sensor, a cuboid of $4.1 \text{ mm} \times 3 \text{ mm} \times 1.15 \text{ mm}$, it is not feasible to place them at each tip of the six poles. Three Hall sensors are, therefore, placed on the top surfaces of the three poles (P2, P4, P5) on the upper plane and the other three on the bottom surfaces of the three poles (P1, P3, P6) on the lower plane. The Hall element within the IC chip is a 0.3 mm diameter plate, which is 0.41 mm to the surface of the chip.

It was experimentally verified that the measurement of the Hall sensor on the surface, denoted as v_s , is proportional to that of a suppositional Hall sensor at the tip, denoted as v_t [28]. It was shown that when applying a sinusoidal input current to P1, the ratio between v_s and v_t remained almost constant (~ 0.47) as the frequency being increased up to 4000Hz. Therefore, a quasi-static relationship is valid up to at least 4000 Hz. The surface-mount Hall sensors can, therefore, be used to measure the magnetic flux at the six tips, i.e., $\Phi = \mathbf{D}_H \mathbf{v}_H$, wherein \mathbf{D}_H is a diagonal voltage-flux gain matrix and \mathbf{v}_H the sensor-voltage

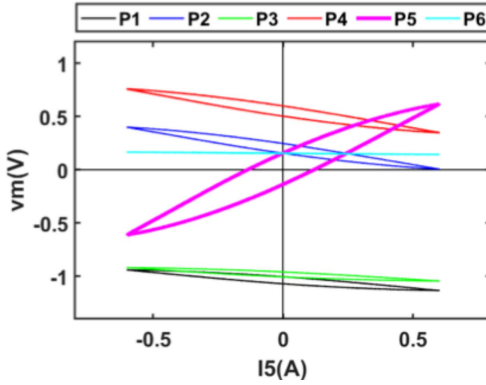


Fig. 2. Flux generation experiment: Multipole coupling; bias; and hysteresis.

vector [29]. Normalizing \mathbf{D}_H , i.e., $\bar{\mathbf{D}}_H = \mathbf{D}_H / \|\mathbf{D}_H\|$, and substituting it into (2), the 3-D magnetic force can be determined

$${}^A\mathbf{f}_m({}^A\mathbf{p}, \mathbf{v}_H) = g_H \sum_{i=1}^6 \sum_{j=1}^6 \bar{\Phi}_i \bar{\Phi}_j \nabla \left(\frac{\mathbf{u}_i \cdot \mathbf{u}_j}{\hat{r}_i^2 \hat{r}_j^2} \right) \quad (5)$$

where $\bar{\Phi} = \bar{\mathbf{D}}_H \mathbf{v}_H$ and $g_H = \|\mathbf{D}_H\|^2$. g_ϕ is the force gain associated with the sensor-voltage vector. Once the force gain, i.e., g_H , and the five independent parameters of $\bar{\mathbf{D}}_H$, being determined via calibration, (5) can be used to calculate the generated force. In addition, optimal voltage allocation can be derived from $\hat{\Phi}_{\text{opt}}(\varphi, \theta, {}^A\hat{\mathbf{p}})$ to implement flux control for force generation

$$\mathbf{v}_{\text{opt}}({}^A\mathbf{f}_d, {}^A\hat{\mathbf{p}}) = \sqrt{\frac{f_d}{g_H}} \bar{\mathbf{D}}_H^{-1} \hat{\Phi}_{\text{opt}}(\varphi, \theta, {}^A\hat{\mathbf{p}}). \quad (6)$$

D. Dynamics of Magnetic Flux Generation

The six Hall sensors were connected to a FPGA board via a six-channel AD converter. The dynamics of flux generation were studied in two experiments. First, a single input current, $I_5 = 0.6 \cdot \sin(0.2\pi t)$ A, was applied to P5 and the voltage readings of the six Hall sensors were recorded and shown in Fig. 2. Three observations are made: since the input current I_5 was used to magnetize P5, it produced a larger flux that converged to the tip of P5 while generating a smaller flux by coupling to each of the other five poles; the resulting flux bias was caused by remanence; and hysteresis is evident.

The frequency response of flux generation was examined in the second experiment. Six single-pole excitations were tested. In each test, the amplitude of the input current is 0.6 A and the frequency was increased from 0.1 to 1.6 kHz. Voltage readings for all six sensors were recorded. The FFT was then used to calculate the discrete frequency spectrum of the six output responses to validate that the dominant frequency be the excitation frequency and to remove the bias caused by remanence. The amplitude ratio and phase lag were then calculated. There were six frequency response tests, each producing six sets of results, one of which is shown in Fig. 3. It is worth noting that the

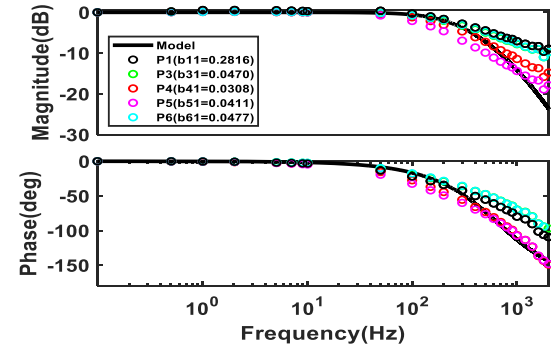


Fig. 3. Normalized magnitude ratio and phase lag of the hexapole actuator subject to first pole excitation. Color circles are experimental results. Black curves are calculated using the fitted dynamic model.

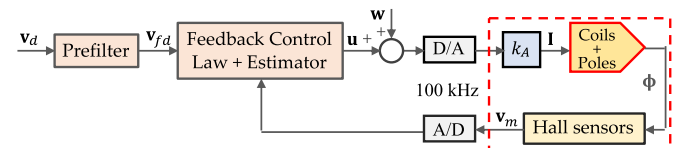


Fig. 4. Block diagram of the six-input-six-output magnetic flux control system.

normalized response of the second pole is not shown in Fig. 3 since it is the least important.

A second order six-input-six-output dynamic model was then fitted using all 36 sets of amplitude ratios and phase lag

$$\mathbf{H}(s) = \frac{1.4848 \times 10^7}{s^2 + 8.1877 \times 10^3 s + 1.4848 \times 10^7} \mathbf{B} \quad (7)$$

where \mathbf{B}

$$= \begin{bmatrix} 0.2816 & -0.0052 & -0.0406 & -0.0305 & -0.0316 & -0.0505 \\ -0.0111 & 0.2659 & -0.0423 & -0.0666 & -0.0756 & -0.0346 \\ -0.0470 & -0.0332 & 0.2795 & -0.0064 & -0.0237 & -0.0550 \\ -0.0308 & -0.0646 & -0.0129 & 0.2348 & -0.0833 & -0.0193 \\ -0.0411 & -0.0661 & -0.0217 & -0.0760 & 0.2537 & -0.0118 \\ -0.0477 & -0.0208 & -0.0402 & -0.0250 & -0.0056 & 0.2302 \end{bmatrix}.$$

It shows that when focusing on the dominant frequency components of the response, the multipole coupling in flux generation can be depicted by a 6×6 matrix, \mathbf{B} , and the dynamic process by an overdamped second order dynamic system with a bandwidth of about 200 Hz.

III. HALL-SENSOR-BASED MAGNETIC FLUX CONTROL

A six-input-six-output magnetic flux control system is designed to achieve precise and high-bandwidth flux generation to precisely control the force applied to the microprobe.

A. Magnetic Flux Control

A six-input-six-output discrete control law is designed and implemented to achieve magnetic flux control. A block diagram of the control system is shown in Fig. 4, where the controlled plant is depicted within the red dashed box and k_A is the amplifier gain. Based on the allocated voltage v_d and Hall-sensor measurement v_m , the flux control law actively adjusts the six actuation currents to control the magnetic flux at the six pole

tips. The control law is an improved version of the previous implementation [29]. Since the magnetic flux control system is a sampled-data system with zero-order-hold and sampling, the discrete model used in the previous implementation is a discrete approximation that is matched over a limited bandwidth.

For the continuous-time process described by $\mathbf{H}(s)$ and preceded by a ZOH, the exact discrete model is derived as $\mathbf{H}(z^{-1}) = (1 - z^{-1})\mathcal{Z}\{\mathbf{H}(s)/s\}$, where \mathcal{Z} is the z-transform of the time series sampled from a continuous time signal whose Laplace transform is the expression in the brace [31]. Using $\mathbf{H}(s)$ in (7) and the sampling rate of 100 kHz, the discrete model of the sampled-data system is

$$\mathbf{H}(z^{-1}) = z^{-1} \frac{7.2126 \times 10^{-4} \times (1 + 0.9731z^{-1})}{(1 - 0.9733z^{-1})(1 - 0.9467z^{-1})} \mathbf{B}. \quad (8)$$

The discrete model shows that the sampled-data system has a delay of one step, two stable poles, and a zero, -0.9731 , close to -1 in the z-plane. It is worth noting that when using a direct digital design special attention needs to be paid to the zero close to -1 to avoid the ringing pole in the discrete control law of the design [32]. According to (8), the dynamic model associated with the control variable is cast as a difference equation

$$\begin{aligned} \mathbf{v}_m[k+1] &= -a_1\mathbf{v}_m[k] - a_2\mathbf{v}_m[k-1] \\ &\quad + k\mathbf{B}(\mathbf{u}[k] + b\mathbf{u}[k-1] + \mathbf{w}[k]) \end{aligned} \quad (9)$$

wherein the joined effect of the modeling error and remanence is presented as a disturbance \mathbf{w} , and a_1, a_2, k , and b are from (8). The goal of magnetic flux control is to control \mathbf{v}_m to track \mathbf{v}_d when affected by \mathbf{w} . The discrete control law consists of three components: a prefilter on the desired voltage \mathbf{v}_d to generate \mathbf{v}_{df} that serves as the reference of the feedback control law, a conventional feedback control law to achieve the desired error dynamics associated with $\delta\mathbf{v} = \mathbf{v}_{df} - \mathbf{v}_m$, and an estimator to provide an estimated disturbance $\hat{\mathbf{w}}$. The control law achieving the control objective is, therefore, expressed as a superposition of \mathbf{u}_{fb} and $\hat{\mathbf{w}}$, i.e., $\mathbf{u}[k] = \mathbf{u}_{fb}[k] - \hat{\mathbf{w}}[k]$.

Since the sampled-data system has a zero, $-b$, close to -1 , when specifying typical error dynamics, i.e., $\delta\mathbf{v}[k+1] = \lambda_c \delta\mathbf{v}[k]$, where $0 \leq \lambda_c < 1$, for a direct digital design a ringing pole will be created. Instead, the desired error dynamics attributed to the reference input are specified as

$$\delta\mathbf{v}_r[k+1] = \lambda_c \delta\mathbf{v}_r[k] + \delta\mathbf{v}_{df}[k+1] \quad (10)$$

where $\delta\mathbf{v}_{df}[k+1] = \mathbf{v}_{df}[k+1] - (1 - b_1)\mathbf{v}_{df}[k] - b_1\mathbf{v}_{df}[k-1]$ and b_1 has to be $(1 - \lambda_c) \cdot b / (1 + b)$ so that the closed-loop system has a zero at $-b$. The feedback control law can be derived accordingly

$$\begin{aligned} \mathbf{u}_{fb}[k] &= (1 - b_1)\mathbf{u}_{fb}[k-1] + b_1\mathbf{u}_{fb}[k-2] \\ &\quad + k_u \cdot \mathbf{B}^{-1} \{ \delta\mathbf{v}[k] + a_1\delta\mathbf{v}[k-1] + a_2\delta\mathbf{v}[k-2] \} \end{aligned} \quad (11)$$

where $k_u = (1 - \lambda_c)/(1 + b)/k$. It is seen that the ringing pole, $-b = -0.9731$, is moved to $-b_1$, where $b_1 \approx (1 - \lambda_c)/2$.

When using the feedback control of the design, the error dynamics attributed to \mathbf{w} are expressed as a set of coupled fourth-order difference equations, hence the design and implementation

of an estimator to directly estimate \mathbf{w} is complicated. To simplify the design of the estimator, \mathbf{w} is converted to \mathbf{w}'

$$\begin{aligned} \mathbf{w}'[k] &= -a_1\mathbf{w}'[k-1] - a_2\mathbf{w}'[k-2] \\ &\quad + \mathbf{B} \{ \mathbf{w}[k] - (1 - b_1)\mathbf{w}[k-1] - b_1\mathbf{w}[k-2] \}. \end{aligned} \quad (12)$$

The resulting error dynamics become

$$\delta\mathbf{v}_w[k+1] = \lambda_c \delta\mathbf{v}_w[k] - k \{ \mathbf{w}'[k] + b\mathbf{w}'[k-1] \}. \quad (13)$$

Letting $\mathbf{w}_1[k] = \mathbf{w}'[k]$ and $\mathbf{w}_2[k] = \mathbf{w}'[k-1]$, and combining (10) and (13) with disturbance compensation, $\delta\mathbf{v} = \delta\mathbf{v}_r + \delta\mathbf{v}_w$, the error dynamics are derived

$$\delta\mathbf{v}[k+1] = \lambda_c \delta\mathbf{v}[k] + \delta\mathbf{v}_{df}[k+1] - k\mathbf{e}_{w_1}[k] - k\mathbf{e}_{w_2}[k] \quad (14)$$

where $\mathbf{e}_{w_1} = \mathbf{w}_1 - \hat{\mathbf{w}}_1$ and $\mathbf{e}_{w_2} = \mathbf{w}_2 - \hat{\mathbf{w}}_2$. The disturbance is modeled as: $\mathbf{w}_1[k+1] = \mathbf{w}_1[k] + \delta\mathbf{w}[k]$, $\delta\mathbf{w}[k+1] = \delta\mathbf{w}[k]$, and $\mathbf{w}_2[k+1] = \mathbf{w}_1[k]$. Since the error dynamics (13) as well as the disturbance model are decoupled, the augmented state estimator [31], [33] is cast in a decoupled format

$$\left\{ \begin{array}{l} \delta\hat{v}_i[k+1] = \lambda_c \delta\hat{v}_i[k] + \delta v_{dfi}[k+1] \\ \quad + \ell_1 \{ \delta v_i[k] - \delta\hat{v}_i[k] \} \\ \hat{w}_{1i}[k+1] = \hat{w}_{1i}[k] + \delta\hat{w}_i[k] \\ \quad + \ell_2 \{ \delta v_i[k] - \delta\hat{v}_i[k] \} \\ \delta\hat{w}_i[k+1] = \delta\hat{w}_i[k] + \ell_3 \{ \delta v_i[k] - \delta\hat{v}_i[k] \} \\ \hat{w}_{2i}[k+1] = \hat{w}_{1i}[k] + \ell_4 \{ \delta v_i[k] - \delta\hat{v}_i[k] \} \end{array} \right. \quad (15)$$

where $i = 1, \dots, 6$ and ℓ 's are the four feedback gains of the estimator. Based on (14) and the disturbance model, the estimation error dynamics is derived

$$\begin{bmatrix} e_{\delta v}[k+1] \\ e_{w_1}[k+1] \\ e_{\delta w}[k+1] \\ e_{w_2}[k+1] \end{bmatrix} = \begin{bmatrix} \lambda_c - \ell_1 & -k & 0 & -kb \\ -\ell_2 & 1 & 1 & 0 \\ -\ell_3 & 0 & 1 & 0 \\ -\ell_4 & 1 & 0 & 0 \end{bmatrix} \begin{bmatrix} e_{\delta v}[k] \\ e_{w_1}[k] \\ e_{\delta w}[k] \\ e_{w_2}[k] \end{bmatrix}. \quad (16)$$

Let all eigenvalues be λ_e , the four feedback gains of the estimator are derived,

$$\left\{ \begin{array}{l} \ell_1 = 2 + \lambda_c - 4\lambda_e \\ \ell_2 = \frac{(\lambda_e - 1)^3(4b + \lambda_e + 3)}{k(b+1)^2} \\ \ell_3 = \frac{-(\lambda_e - 1)^4}{k(b+1)} \\ \ell_4 = \frac{(\lambda_e^4 + 4b\lambda_e^3 + 6b^2\lambda_e^2 - 4b(2b+1)\lambda_e + 3b^2 + 2b)}{bk(b+1)^2} \end{array} \right. . \quad (17)$$

Using the inverse conversing of (12), the estimated $\hat{\mathbf{w}}'$, which is $\hat{\mathbf{w}}_1$, is converted to $\hat{\mathbf{w}}$ for disturbance compensation

$$\begin{aligned} \hat{\mathbf{w}}[k] &= (1 - b_1)\hat{\mathbf{w}}[k-1] + b_1\hat{\mathbf{w}}[k-2] + \mathbf{B}^{-1} \{ \hat{\mathbf{w}}_1[k] \\ &\quad + a_1\hat{\mathbf{w}}_1[k-1] + a_2\hat{\mathbf{w}}_1[k-2] \}. \end{aligned} \quad (18)$$

Applying the control law, $\mathbf{u}[k] = \hat{\mathbf{u}}_{fb}[k] - \hat{\mathbf{w}}[k]$, where $\hat{\mathbf{u}}_{fb}$ is determined by replacing $\delta\mathbf{v}$ in (11) with $\delta\hat{\mathbf{v}}$, the closed-loop response of magnetic flux control is derived from (14)

$$\begin{aligned} \mathbf{v}_m[k+1] &= \lambda_c \mathbf{v}_m[k] + \frac{1 - \lambda_c}{1 + b} \{ \mathbf{v}_{df}[k] + b\mathbf{v}_{df}[k-1] \} \\ &\quad + k\mathbf{e}_{w_1}[k] + k\mathbf{e}_{w_2}[k]. \end{aligned} \quad (19)$$

The prefilter is designed to further improve the control of magnetic flux for high-speed applications. Using (19) and referring to the design of feedforward controllers for nonminimum phase systems [34], [35], a prefilter is designed

$$\begin{aligned} \mathbf{v}_{df}[k] = & \frac{1}{(1 - \lambda_c)(1 + b)} \left\{ b\mathbf{v}_d[k + d] \right. \\ & \left. + (1 - b\lambda_c)\mathbf{v}_d[k + d - 1] - \lambda_c\mathbf{v}_d[k + d - 2] \right\} \end{aligned} \quad (20)$$

where d is the number of preview steps. Ignoring the estimation error, the response of magnetic flux control is

$$\begin{aligned} \mathbf{v}_m[k + 1] = & \frac{1}{(1 + b)^2} \left\{ b\mathbf{v}_d[k + d - 1] \right. \\ & \left. + (1 + b^2)\mathbf{v}_d[k + d - 2] + b\mathbf{v}_d[k + d - 3] \right\}. \end{aligned} \quad (21)$$

The frequency response of the control system with prefiltering is derived, i.e., $[(1 + 2b \cdot \cos \theta + b^2)/(1 + b)^2]e^{j(d-2)\theta}$, where $\theta = \omega\Delta t$ and $\Delta t = 10^{-5}$ seconds. It is evident that when $d = 2$, the phase error of the response is zero. As can be seen, the system has a unity steady-state gain that drops to 0.707 at 20 kHz. The control law along with the augmented estimator and the prefilter is used to achieve three objectives, i.e., minimizing the uncertainty attributed to magnetic remanence and hysteresis, increasing the bandwidth of magnetic flux generation, and eliminating multipole coupling within the bandwidth of interest. They are implemented using a high-speed FPGA system (Altera: Arria V GT) for real-time computation.

Three set of experimental results are presented below to verify the effectiveness of flux control. In each experiment, the desired force and the position of the probe are first specified in the measurement coordinate, ${}^M\mathbf{f}_d$ and ${}^M\mathbf{p}$, converted to the actuator coordinate, ${}^A\mathbf{f}_d$ and ${}^A\mathbf{p}$, then \mathbf{v}_{opt} obtained by optimal voltage allocation (6) to serve as the input of the flux control system, i.e., \mathbf{v}_d . The real-time computation for coordinate transformation and optimal voltage allocation operates at a frequency of 1.6 kHz, while the flux control is 100 kHz. The output of flux control, \mathbf{v}_m , is then used to calculate the 3-D magnetic force, ${}^M\mathbf{f}_m$, in real time or via batch processing.

B. Elimination of Bias and Hysteresis

Two experiments were used to demonstrate the effectiveness of closed-loop flux control. In both experiments, the desired force was a sinusoidal function, $f_d(t) = 5 \cdot \sin(100\pi t)pN$, along a specified direction. Voltage allocation was converted to current allocation, i.e., $\mathbf{I} = \mathbf{K}_I^{-1}\mathbf{D}_H\mathbf{v}_d$, to realize current based flux generation in the first experiment, whereas optimal voltage allocation along with closed-loop flux control was used to control magnetic flux generation in the second experiment. The six Hall-sensor voltage readings, \mathbf{v}_m , were recorded and used to calculate the resulting 3-D magnetic force.

The comparison of experimental results is shown in Fig. 5, where the desired force is along the z -axis. The upper panel

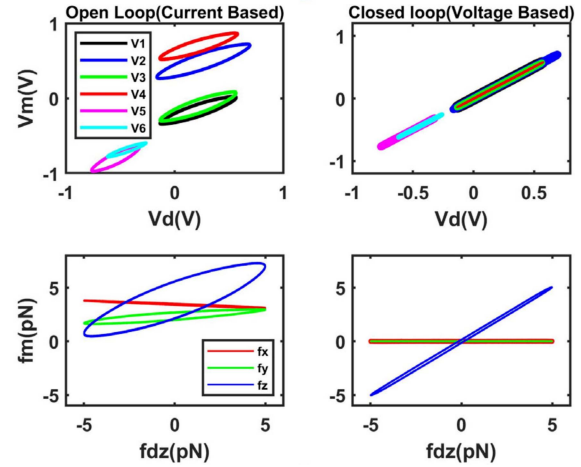


Fig. 5. Upper panel shows the comparison of sinusoidal magnetic flux generation, six components of the measured sensor voltage \mathbf{v}_m versus the desired voltage \mathbf{v}_d . The lower panel shows sinusoidal magnetic force generation, three components of the 3-D output magnetic force \mathbf{f}_m versus the desired magnetic force \mathbf{f}_{dz} .

shows that the bias, caused by magnetic remanence, and hysteresis/phase lag in flux generation were minimized by closed-loop flux control. The lower panel shows that multi-axis coupling and hysteresis/phase lag in 3-D force generation were significantly reduced by optimal voltage allocation and closed-loop magnetic flux control. Similar results were obtained when the desired force was generated in different other directions.

C. Frequency Response of Magnetic Flux Control

The frequency response of the six-input-six-output magnetic flux control system was experimentally evaluated. In each experiment, the amplitude of the desired voltage associated with a single pole was set to be 2V and the frequency was increased from 0.1 to 4 kHz. The value of λ_c associated with the control law is 0.8179 (3200 Hz), that of λ_e for the estimator 0.3659 (16000 Hz), and the number of preview steps is zero, $d = 0$. The voltage readings of all six Hall sensors were recorded. The magnitude ratio and phase lag were then calculated to form frequency response curves. Fig. 6 shows the frequency response curves of \mathbf{v}_m associated with the six pole tips when the desired voltage for P5 is 2V and those for the other five poles are zeros. It is seen that while the hexapole actuator has multipole coupling, uncertainties caused by magnetic remanence and hysteresis, and limited bandwidth, with the improved six-input-six-output flux control, the magnetic flux at each pole tip can be individually and precisely controlled at frequencies over 4 kHz without any experimental tuning. More importantly, the experimental results precisely followed the theoretical predictions based on the design. Similar results were obtained when different individual pole was selected in the experiment. It shows that while the hexapole actuator has multipole coupling, uncertainties caused by magnetic remanence and hysteresis, and limited bandwidth, with six-input-six-output magnetic flux control, the magnetic flux at each pole tip can be individually, accurately controlled

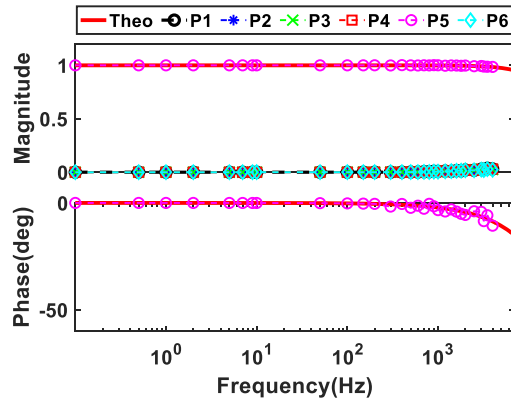


Fig. 6. Frequency response curves of six-axis magnetic flux control are compared with the theoretical predictions based on the design.

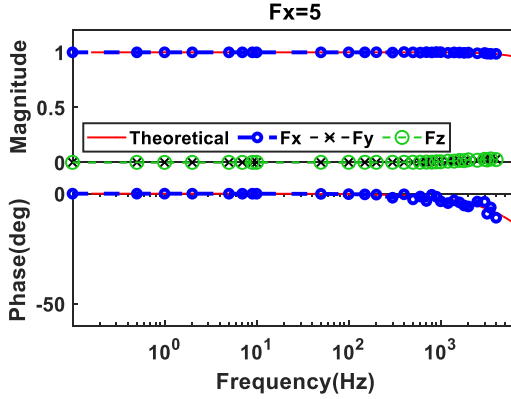


Fig. 7. Frequency response curves of the three-axis magnetic force generation are compared with the theoretical predictions based on the design.

at frequencies up to 4 kHz. In addition, the experimental results accord well with the theoretical predictions.

D. Frequency Response of Magnetic Force Generation

The frequency response of the three-input-three-output magnetic force generation system was experimentally evaluated. In each experiment, with the preselected amplitude and direction of the desired force, the frequency was increased from 0.1 Hz to 4 kHz. The voltage readings of all six Hall sensors were recorded and used to calculate the resulting magnetic force to form frequency response curves. Fig. 7 shows the frequency response curves of the three-axis output force when the desired force is 5 pN along the x-axis. When the magnitude of the desired force was increased to 10 pN, the obtained frequency response curves are fully accord with those shown in Fig. 7. In addition, the experimental results are in good agreement with the theoretical predictions. Similar results were obtained when the y-axis or the z-axis was selected in the experiment. The results show that together with the optimized flux allocation, the developed flux control system generates precise magnetic forces, making the six-input hexapole system behave like a decoupled three-axis force generator with a bandwidth of more than 4 kHz.

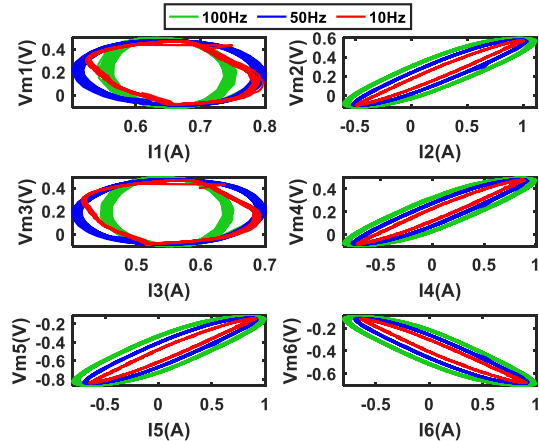


Fig. 8. Hysteresis and multipole coupling in hexapole current actuation.

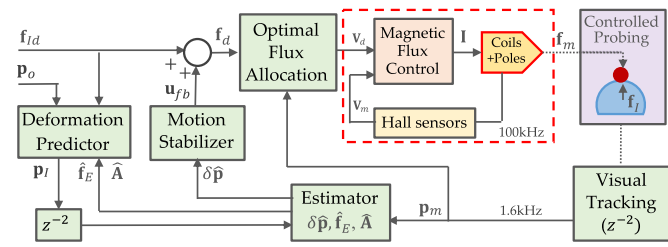


Fig. 9. Block diagram of probe-sample interaction force control.

Fig. 8 uses three set of data from the frequency response experiments at 10, 50, and 100 Hz (see Fig. 7) to show the relationship between the input current and output sensor voltage reading. It shows that the hysteresis (ten cycles) and multipole coupling associated with hexapole current actuation are significant. Nonetheless, it verifies that the flux control law could actively adjust the six input currents to control the magnetic flux at the six tips of the hexapole actuator to follow the desired value v_d to precisely generate the desired magnetic force f_d .

IV. CONTROL OF PROBE-SAMPLE INTERACTION

Fig. 9. shows the block diagram of probe-sample interaction force control by a magnetic microprobe in aqueous solution, wherein f_{Id} is the desired interaction force and p_o is the position of the probe at the beginning of the probing process. The desired interaction force f_{Id} , points to the negative surface normal direction of the sample while its direction remains unchanged during each probing process.

When a magnetic force is applied to the probe to indent the sample surface, an interaction force is formed, resulting in a nonlinear dynamic indentation response. Since this nonlinear response depends on a priori unknown mechanical properties of the sample, process parameters need to be estimated in real time. Interaction force control includes three components: the parameter estimator that estimates time-varying indentation gain and elastic force in real time; the deformation predictor that uses the estimated parameters to predict the sample deformation; and

the motion stabilizer that stabilizes the probe with the expected sample deformation, \mathbf{p}_I . Motion stabilization is achieved using a feedback control law. Therefore, the required control force, \mathbf{f}_d , is a superposition of the desired interaction force and the feedback control effort, i.e., $\mathbf{f}_d = \mathbf{f}_{Id} + \mathbf{u}_{fb}$. Through optimal flux allocation and closed-loop flux control, the magnetic force is precisely generated, $\mathbf{f}_m = \mathbf{f}_d$.

A. Modeling and Control of Sample Indentation

For simplicity, the following analysis focuses on the control of the interaction force along the z -axis. The results can be applied to any uniaxial force control. When being in contact with the sample, in addition to thermal force, two more forces are applied to the probe, namely the magnetic force and the interaction force. Since the probe continues to move within the sampling interval, these two forces vary with the motion of the probe. Using the zero-order-hold to realize digital control, for $k\Delta t \leq t < (k+1)\Delta t$, the first order Taylor expansion is used to approximate the position-dependent magnetic force, f_{mz} , as well as the resulting interaction force, f_{Iz} , between the probe and the sample, which is modeled as an object having nonlinear viscoelastic properties

$$\begin{cases} f_{mz}(z(t), \mathbf{v}_d) \approx f_{mz}[k] + k_{mz}[k]\delta z(t) \\ f_{Iz}(t) \approx f_E[k] + k_s[k]\delta z(t) + \gamma_s[k]\delta \dot{z}(t) \end{cases} \quad (22)$$

where $f_{mz}[k] = f_{mz}(z[k], \mathbf{v}_d[k])$ is the magnetic force at $t = k\Delta t$, $k_{mz}[k] = -(\partial f_{mz}/\partial z)|_{z[k], \mathbf{v}_d[k]}$, $f_E[k]$ is the elastic force at $t = k\Delta t$, $k_s[k]$ is the elastic force coefficient, and $\gamma_s[k]$ is the damping coefficient. Both k_s and γ_s are deformation-dependent mechanical properties of the sample.

From (1), the movement of the probe within the sampling interval is governed by the following equation:

$$\gamma_z[k]\delta \dot{z}(t) = -k_z[k]\delta z(t) + \{f_{mz}[k] - f_E[k] + f_{Tz}[k]\}, \quad (23)$$

where $\gamma_z[k] \approx \gamma_s[k]$ is the unknown viscous damping coefficient, $k_z[k] = k_s[k] - k_{mz}[k] \approx k_s[k]$ is the unknown elastic force coefficient, and $f_{Tz}[k]$ is the thermal force. The dynamic equation can then be converted to a difference equation

$$z[k+1] = z[k] + a_z[k] \{f_{mz}[k] - f_E[k] + f_{Tz}[k]\} \quad (24)$$

where the indentation gain is

$$a_z[k] = \left\{ 1 - \exp \left(-\frac{k_z[k]}{\gamma_z[k]}\Delta t \right) \right\} / k_z[k]. \quad (25)$$

It is worth noting that in the absence of probe-sample interaction $k_z[k] = -k_{mz}[k]$, which is thought of as a negative spring constant that causes instability. When using feedback control to stabilize the probe, the effect of the negative spring over a sampling period is negligible as the Δt is small, and $a_z[k]$ in (25) can be approximated as $a_z[k] = \Delta t/\gamma_z$. However, $a_z[k]$ is significantly reduced with probe-sample interaction.

With the estimated indentation gain and the estimated elastic force, the predicted motion of the probe is governed by

$$z_I[k+1] = z_I[k] + \hat{a}_z[k] \left\{ f_{Idz}[k] - \hat{f}_E[k] \right\}. \quad (26)$$

Using proportional control, $f_{dz}[k] = f_{Idz}[k] + k_p\delta z_m[k]$, where k_p is the control gain and $\delta z_m[k] = z_I[k-2] - z_m[k]$. Through optimal flux allocation and closed-loop flux control, the magnetic force is precisely generated, $f_{mz}[k] = f_{dz}[k]$. Since $z_m[k] = z[k-2] + n_z[k]$, where $n_z[k]$ is measurement noise, the dynamic equation with feedback control is derived from (24)

$$\begin{aligned} z[k+1] = z[k] + a_z[k] &\{f_{Idz}[k] + k_p\delta z[k-2] - f_E[k]\} \\ &+ a_z[k] \{k_p n_z[k] + f_{Tz}[k]\}. \end{aligned} \quad (27)$$

Comparing (26) and (27), the equation of motion error, $\delta z[k] = z_I[k] - z[k]$, is derived

$$\begin{aligned} \delta z[k+1] = \delta z[k] - \hat{a}_z[k]k_p\delta z[k-2] - \hat{f}_D[k]e_{a_z}[k] \\ - \hat{a}_z[k]e_{f_E}[k] - a_z[k]r_z[k] \end{aligned} \quad (28)$$

where \hat{a}_z is the estimate of a_z , $e_{a_z} = a_z - \hat{a}_z$ is the estimation error, \hat{f}_E is the estimate of f_E , $e_{f_E} = f_E - \hat{f}_E$ is the estimation error, $\hat{f}_D[k] = \{k_p\delta z[k-2] + f_{Idz}[k] - \hat{f}_E[k]\}$ is the estimate of f_D , and $r_z[k] = k_p n_z[k] + f_{Tz}[k]$ is random excitation. It is seen that when the estimation errors are negligible, $e_{a_z} \approx 0$ and $e_{f_E} \approx 0$, the probe moves with the expected deformation z_I . Since the motion error δz is the output of a linear system, (28), driven by random force, $r_z[k]$, attributed to thermal force and measurement noise, the motion error is zero-mean random error. Therefore, the generated magnetic force has two components, i.e.,

$$f_{mz}[k] = f_{det}[k] + f_{ran}[k] \approx f_{Idz}[k] + k_p\delta z_m[k] \quad (29)$$

wherein the deterministic component follows the desired interaction force without error, $f_{det}[k] = f_{Idz}[k]$, and the random component has a theoretically predictable variance, i.e., $var(f_{ran}) = k_p^2 \{var(\delta z) + \sigma_{n_z}^2\}$.

It is worth noting that thermal noise and measurement noise are coupled to the generated magnetic force through feedback control. Therefore, when force generation is the objective, a smaller feedback gain k_p is used to reduce the feedback control force and thus the random component of the magnetic force. In addition, if the expected deformation z_I is not used in the control law, the motion error, $\delta z[k] = z_o - z[k]$, is no longer a zero-mean random error. Thus, deterministic force error, caused by the deterministic force, $\{-f_{Idz}[k] + f_E[k]\}$, is expected.

B. Real-Time Estimation of Process Parameters

Real-time estimation of the elastic force and the indentation gain is required to achieve the desired indentation control. Due to the two-step measurement delay, $\delta z[k-2]$ appears in (28) through feedback control, therefore, three variables, $\delta z_1[k] = \delta z[k-2]$, $\delta z_2[k] = \delta z[k-1]$, and $\delta z_3[k] = \delta z[k]$, are used to model the dynamics of motion error. In addition, the elastic force and the input gain are modeled by two separate second-order processes, respectively. Thus, a process model with seven variables is used to depict the true state of the seven variables at time k

evolved from the state at $(k - 1)$

$$\left\{ \begin{array}{l} \delta z_1[k+1] = \delta z_2[k] \\ \delta z_2[k+1] = \delta z_3[k] \\ \delta z_3[k+1] = -\hat{a}_z[k]k_p\delta z_1[k] + \delta z_3[k] - \hat{f}_D[k]e_{az}[k] \\ \quad - \hat{a}_z[k]e_{f_E}[k] - a_z[k]r_z[k] \\ f_E[k+1] = f_E[k] + \delta f_E[k] \\ \delta f_E[k+1] = \delta f_E[k] \\ a_z[k+1] = a_z[k] + \delta a_z[k] \\ \delta a_z[k+1] = \delta a_z[k] \end{array} \right. \quad (30)$$

where $a_z[k]r_z[k]$ is the process noise. At time k the available measurement is $\delta z_m[k]$, which is separated into two components by a real-time algorithm. The determinist component serves as a measurement of $\delta z_1[k]$ and the variance of the random component is used to calculate $a_z[k - 2]$. Therefore, the output matrix of the process is a 2×7 matrix

$$\mathbf{H} = \begin{bmatrix} 1 & 0 & 0 & 0 & 0 & 0 & 0 \\ 0 & 0 & 0 & 0 & 0 & 1 & 0 \end{bmatrix}. \quad (31)$$

With a 7×2 feedback matrix, $\mathbf{L}[k]$, the estimator is cast as

$$\left\{ \begin{array}{l} \delta \hat{z}_1[k+1] = \delta \hat{z}_2[k] + \{\ell_{11}[k]e_{z_1}[k] + \ell_{12}[k]e_{a_z}[k]\} \\ \delta \hat{z}_2[k+1] = \delta \hat{z}_3[k] + \{\ell_{21}[k]e_{z_1}[k] + \ell_{22}[k]e_{a_z}[k]\} \\ \delta \hat{z}_3[k+1] = -\hat{a}_z[k]k_p\delta \hat{z}_1[k] + \delta \hat{z}_3[k] \\ \quad + \{\ell_{31}[k]e_{z_1}[k] + \ell_{32}[k]e_{a_z}[k]\} \\ \hat{f}_{Iz}[k+1] = \hat{f}_{Iz}[k] + \delta \hat{f}_{Iz}[k] \\ \quad + \{\ell_{41}[k]e_{z_1}[k] + \ell_{42}[k]e_{a_z}[k]\} \\ \delta \hat{f}_{Iz}[k+1] = \delta \hat{f}_{Iz}[k] + \{\ell_{51}[k]e_{z_1}[k] + \ell_{52}[k]e_{a_z}[k]\} \\ \hat{a}_z[k+1] = \hat{a}_z[k] + \delta \hat{a}_z[k] \\ \quad + \{\ell_{61}[k]e_{z_1}[k] + \ell_{62}[k]e_{a_z}[k]\} \\ \delta \hat{a}_z[k+1] = \delta \hat{a}_z[k] + \{\ell_{71}[k]e_{z_1}[k] + \ell_{72}[k]e_{a_z}[k]\} \end{array} \right. \quad (32)$$

where $\ell[k]$'s are entries of $\mathbf{L}[k]$, $e_{z_1}[k] = \delta z_1[k] - \delta \hat{z}_1[k]$ and $e_{a_z}[k] = a_z[k - 2] - \hat{a}_z[k]$. Comparing (30) and (32), the dynamic of estimation errors, \mathbf{e} , is derived

$$\mathbf{e}[k+1] = \mathbf{F}_e[k]\mathbf{e}[k] - \mathbf{L}[k]\mathbf{H}\mathbf{e}[k] + \mathbf{r}[k] \quad (33)$$

where $\mathbf{r}[k]$ is the process noise attributed to $a_z[k]r_z[k]$ and $\mathbf{F}_e[k]$ is the state transition matrix

$$\mathbf{F}_e[k] = \begin{bmatrix} 0 & 1 & 0 & 0 & 0 & 0 & 0 \\ 0 & 0 & 1 & 0 & 0 & 0 & 0 \\ -\hat{a}_z[k]k_p & 0 & 1 & -\hat{a}_z[k] & 0 & -\hat{f}_D[k] & 0 \\ 0 & 0 & 0 & 1 & 1 & 0 & 0 \\ 0 & 0 & 0 & 0 & 1 & 0 & 0 \\ 0 & 0 & 0 & 0 & 0 & 1 & 1 \\ 0 & 0 & 0 & 0 & 0 & 0 & 1 \end{bmatrix}. \quad (34)$$

With $\mathbf{F}_e[k]$ and \mathbf{H} , $\mathbf{L}[k]$ is updated by the standard recursive calculation used in the Kalman filtering method [31], [36], wherein the covariance matrix, $\mathbf{Q}[k]$, of the process noise is related to the variance of thermal force and that of measurement noise according to $a_z[k]r_z[k] \approx \hat{a}_z[k]\{k_p n_z[k] + f_{Tz}[k]\}$, and the covariance matrix, $\mathbf{R}[k]$, of the measurement noise is derived from the variance of n_z . Since $e_{a_z}[k] = a_z[k - 2] - \hat{a}_z[k]$, the estimated input gain has a delay of two steps.

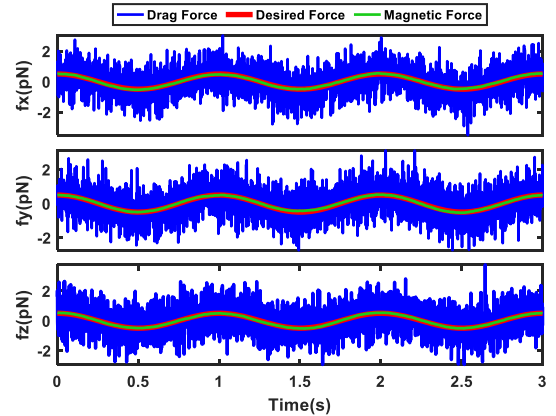


Fig. 10. Magnetic force is compared with the drag force and the desired force.

C. Experimental Verification of Force Generation Accuracy

The normalized flux gain matrix and the probe-specific force gain were determined via experimental calibration, i.e., $\bar{\mathbf{D}}_H = \text{diag}(0.444, 0.364, 0.445, 0.436, 0.353, 0.436)$ and $g_H = 4.741(pN/V^2)$ for the spherical magnetic probe with a radius of $2.25 \mu\text{m}$. They are used to realize optimal voltage allocation using (6) and to calculate the magnetic force from Hall-sensor voltage using (5). However, the accuracy of (5), hexapole magnetic force model, needs to be experimentally verified.

The control system was applied to stabilize the probe in water and control the interaction force between the probe and the surrounding water. Since there is no elastic force in probe-sample interaction, the probe motion, driven by the magnetic force \mathbf{f}_m and subject to random thermal force \mathbf{f}_T , is governed by $\gamma \dot{\mathbf{p}} = \mathbf{f}_m + \mathbf{f}_T$, wherein \mathbf{f}_E in (1) removed. The linear relationship, i.e., $\mathbf{f}_D = \gamma \dot{\mathbf{p}}$, is used to calculate the drag force by measuring the probe's velocity. In the experimental setup, the CMOS camera has high photosensitivity and superior signal to noise ratio. It has been experimentally verified that when using a $60\times$ magnification lens, the measurement resolution for a spherical probe with a radius of $2.25 \mu\text{m}$ is about 0.7 nm (rms) in both the x - and y -directions, and 2.3 nm (rms) in the z -direction [37].

Three experiments were used to verify the accuracy of force generation. First, the probe was stabilized at the center of the workspace using $k_p = 0.1(pN/\mu\text{m})$, each of the three components of the desired force was set to be 0.5 pN and oscillating at 1 Hz . The resulting magnetic force \mathbf{f}_m is compared with the drag force \mathbf{f}_D and the desired force \mathbf{f}_{Id} in Fig. 10. It is seen that \mathbf{f}_m accord well with \mathbf{f}_{Id} . Since $\mathbf{f}_D = \mathbf{f}_m + \mathbf{f}_T$, the mean and standard deviation of $\{\mathbf{f}_D[k] - \mathbf{f}_m[k]\}$ was calculated, i.e., $\sigma_{\delta f_x} = 1.0822 \text{ pN}$, $\sigma_{\delta f_y} = 1.0820 \text{ pN}$, and $\sigma_{\delta f_z} = 1.1170 \text{ pN}$. It is verified that the mean of all three components is very close to zero and the standard deviation is very close to the theoretical values of the thermal force, i.e., $\sigma_{f_{Tx,y}} = 1.0817 \text{ pN}$ and $\sigma_{f_{Tz}} = 1.1153 \text{ pN}$.

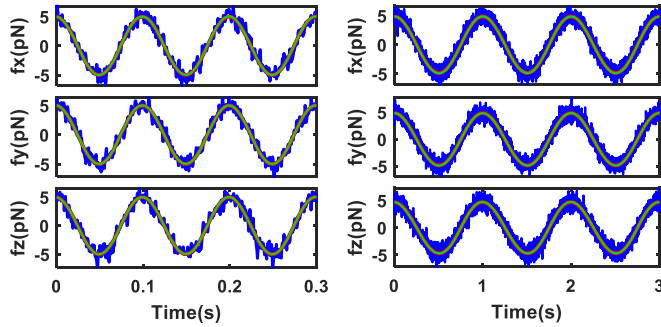


Fig. 11. As in Fig. 10, the left panel compares the resulting magnetic force with the drag force and the desired force in the second experiment and the right panel compares the resulting magnetic force with the drag force and the desired force in the third experiment.

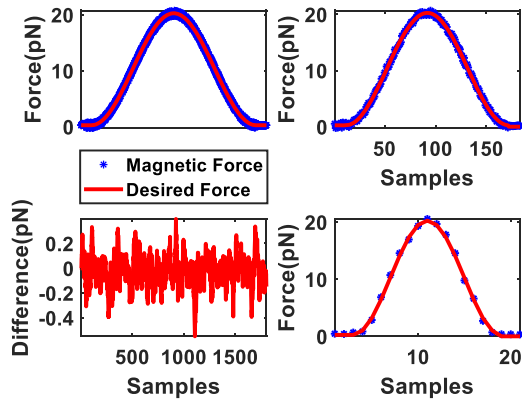


Fig. 12. Comparison between the magnetic force and the desired force in live-cell indentation experiments.

Second, the magnitude of the desired force was increased to 5 pN and the frequency increased to 10 Hz. The comparison is shown in the left panel of Fig. 11. The probe was then stabilized at (30 μm 30 μm 15 μm) in the third experiment. The magnitude and frequency of the desired force were 5 pN and 1 Hz, respectively. The comparison is shown in the right panel of Fig. 11. It is worth noting that the magnetic force (green) is on top of the desired force (red). Both comparisons verify the accuracy of magnetic force generation and that of the hexapole flux-based magnetic force model.

D. Experimental Verification of Interaction Force Control

The control system was applied to control the probe to indent the top surface of a live cell in the negative z direction. Three experiments were performed, in which the desired forces were $f_{Idz}(t) = 10(pN) \times (1 + \cos \omega t)$ at three distinct frequencies, namely 1, 10, and 100 Hz. The force control loop has a sampling frequency of 1.6 kHz. Six Hall-sensor voltages are used to calculate the magnetic force $f_{mz}[k]$ using (5), which are compared with the desired force $f_{Idz}[k]$, as shown in Fig. 12. The top left panel shows the comparison of samples from the 1 Hz indentation experiment with the desired interaction force. It is worth noting that the probe was stabilized on the cell surface

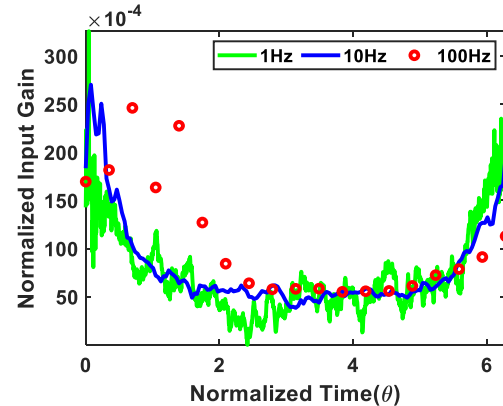


Fig. 13. Input gain estimated in three live-cell indentation experiments.

with a contact force of 0.5 pN preceding the indentation and stabilized at the separation point proceeding the indentation. In between, there are exactly 1600 samples associated with the indentation cycle.

The bottom left panel shows the difference between the magnetic force and the desired force. The results verify that the deterministic component of the magnetic force accords well with the desired force and the difference is close to random error. The top right panel shows the comparison from the 10 Hz experiment, while the bottom right panel shows the comparison from the 100 Hz experiment. It is worth noting that the standard deviation of the force error for all three experiments is about 0.1 pN , which is less than 10% of the thermal force. Since the interaction force is a superposition of magnetic force and thermal forces, control of interaction force is mainly limited by thermal forces.

Fig. 13 shows the input gain estimated in real time in the three live-cell indentation experiments. The temporal variable is normalized, i.e., $\theta = \omega t$, to plot three set of results of the three experiments with distinct time scales in the same plot. The results show that the input gain reduced as the elastic force coefficient of the cell increased with surface deformation. The result from the 100 Hz indentation experiment clearly shows that the estimation of input gain has a delay of two steps.

V. CONCLUSION AND DISCUSSION

A force control system has been designed and developed to accurately generate the 3-D magnetic force exerted on a magnetic microprobe in aqueous solutions under a microscope and precisely control the probe-sample interaction force at the piconewton scale. Accurate force generation was achieved through magnetic flux control, wherein a six-input-six-output digital control law and a disturbance estimator were designed and implemented using a high-speed FPGA system for real-time computation operating at 100 kHz.

Experiments have shown that whereas the hexapole actuator has multipole coupling, uncertainties caused by magnetic remanence and hysteresis, and limited bandwidth, the control system is able to actively adjust the six input currents to accurately control the magnetic flux at each individual pole tips to follow

the desired values at frequencies above 4 kHz. In addition, the experimental results accord well with the theoretical predictions. Moreover, together with optimal flux allocation, the flux control system has been used to render accurate magnetic force generation. It enables the six-input hexapole system to behave like a decoupled three-axis force producer with high bandwidth.

The second function of the control system has been designed and implemented to control the interaction force between the probe and the sample. It has been theoretically proven that when the estimation errors are negligible, the resulting magnetic force has two components. The deterministic component precisely follows the desired interaction force, and the random component has a theoretically predictable variance. The control system was applied to stabilize and move the probe in water, wherein the resulting drag force has been used to verify the accuracy of three-dimensional magnetic force generation, ranging from subpiconewtons to ten piconewtons, at the center and away from the center of the workspace.

The control system was applied to control the probe to indent the top surface of a live cell at three distinct frequencies. Experimental results have verified that the deterministic component of the magnetic force accords well with the desired force and the difference is close to random error. The developed control system enables the hexapole actuator to generate accurate magnetic force to precisely control the interaction of the microprobe with the sample. The functions of the control system form the basis for automatic probing and controlled manipulation of active biological samples in aqueous solutions.

REFERENCES

- [1] Z. P. Zhang and C. H. Menq, "Six-axis magnetic levitation and motion control," *IEEE Trans. Robot.*, vol. 23, no. 2, pp. 196–205, Apr. 2007.
- [2] S. K. Kuo, X. Shan, and C. H. Menq, "Large travel ultra precision X-Y-theta motion control of a magnetic suspension stage," *IEEE/ASME Trans. Mechatron.*, vol. 8, no. 3, pp. 334–341, Sep. 2003.
- [3] L. Zhang, J. J. Abbott, L. X. Dong, B. E. Kratochvil, D. Bell, and B. J. Nelson, "Artificial bacterial flagella: Fabrication and magnetic control," *Appl. Phys. Lett.*, vol. 94, pp. 064107-1–064107-3, 2009.
- [4] X. Wu, J. Liu, C. Huang, M. Su, and T. Xu, "3-D path following of helical microswimmers with an adaptive orientation compensation model," *IEEE Trans. Automat. Sci. Eng.*, vol. 17, no. 2, pp. 823–832, Apr. 2020, doi: [10.1109/TASE.2019.2947071](https://doi.org/10.1109/TASE.2019.2947071).
- [5] L. Zheng et al., "3D navigation control of untethered magnetic microrobot in centimeter-scale workspace based on field-of-view tracking scheme," *IEEE Trans. Robot.*, vol. 38, no. 3, pp. 1583–1598, Jun. 2022, doi: [10.1109/TRO.2021.3118205](https://doi.org/10.1109/TRO.2021.3118205).
- [6] Y. Jeong, G. R. Jayanth, S. M. Jhiang, and C. H. Menq, "Design and fabrication of an active multi-axis probing system for high-speed atomic force microscopy," *IEEE Trans. Nanotechnol.*, vol. 9, no. 3, pp. 392–399, May 2010.
- [7] G. R. Jayanth and C. H. Menq, "Two-axis force sensing and control of a re-orientable scanning probe," *IEEE/ASME Trans. Mechatron.*, vol. 18, no. 2, pp. 687–696, Apr. 2013.
- [8] M. P. Kumar, J. J. Abbott, B. E. Kratochvil, R. Borer, A. Sengul, and B. J. Nelson, "OctoMag: An electromagnetic system for 5-DOF wireless micromanipulation," *IEEE Trans. Robot.*, vol. 26, no. 6, pp. 1006–1017, Dec. 2010.
- [9] C. Bergeles, B. E. Kratochvil, and B. J. Nelson, "Visually servoing magnetic intraocular microdevices," *IEEE Trans. Robot.*, vol. 28, no. 4, pp. 798–809, Aug. 2012.
- [10] X. Zhang, H. Kim, and M. J. Kim, "Design, implementation, and analysis of a 3-D magnetic tweezer system with high magnetic field gradient," *IEEE Trans. Instrum. Meas.*, vol. 68, no. 3, pp. 680–687, Mar. 2019, doi: [10.1109/TIM.2018.2857082](https://doi.org/10.1109/TIM.2018.2857082).
- [11] D. Li, F. Niu, J. Li, X. Li, and D. Sun, "Gradient-enhanced electromagnetic actuation system with a new core shape design for microrobot manipulation," *IEEE Trans. Ind. Electron.*, vol. 67, no. 6, pp. 4700–4710, Jun. 2020, doi: [10.1109/TIE.2019.2928283](https://doi.org/10.1109/TIE.2019.2928283).
- [12] J. Lee, X. Zhang, C. H. Park, and M. J. Kim, "Real-time teleoperation of magnetic force-driven microrobots with 3D haptic force feedback for micro-navigation and micro-transportation," *IEEE Robot. Automat. Lett.*, vol. 6, no. 2, pp. 1769–1776, Apr. 2021, doi: [10.1109/LRA.2021.3060708](https://doi.org/10.1109/LRA.2021.3060708).
- [13] K. C. Neuman and A. Nagy, "Single-molecule force spectroscopy: Optical tweezers, magnetic tweezers and atomic force microscopy," *Nature Methods*, vol. 5, no. 6, pp. 491–505, Jun. 2008.
- [14] J. T. Finer, R. M. Simmons, and J. A. Spudich, "Single myosin molecule mechanics—Piconewton forces and nanometer steps," *Nature*, vol. 368, no. 6467, pp. 113–119, Mar. 1994.
- [15] P. Cluzel et al., "DNA: An extensible molecule," *Science*, vol. 271, no. 5250, pp. 792–794, Feb. 1996.
- [16] J. Zlatanova and S. H. Leuba, "Magnetic tweezers: A sensitive tool to study DNA and chromatin at the single-molecule level," *Biochem. Cell Biol.*, vol. 81, pp. 151–159, 2003.
- [17] C.-H. Chiou, Y.-Y. Huang, M.-H. Chiang, H.-H. Lee, and G.-B. Lee, "New magnetic tweezers for investigation the mechanical properties of single DNA molecules," *Nanotechnology*, vol. 17, pp. 1217–1224, 2006.
- [18] N. Walter, C. Selhuber, H. Kessler, and J. P. Spatz, "Cellular unbinding forces of initial adhesion processes on nanopatterned surfaces probed with magnetic tweezers," *Nano Lett.*, vol. 6, no. 3, pp. 398–402, Mar. 2006.
- [19] D. Salas, V. Gocheva, and M. Nöllmann, "Constructing a magnetic tweezer to monitor RNA translocation at the single-molecule level," in *RNA Remodeling Proteins*, Berlin, Germany: Springer, 2015, pp. 257–273.
- [20] J. K. Fisher et al., "Thin-foil magnetic force system for high-numerical-aperture microscopy," *Rev. Sci. Instrum.*, vol. 77, 2006, Art. no. 023702.
- [21] Z. P. Zhang, Y. N. Huang, and C. H. Menq, "Actively controlled manipulation of a magnetic microbead using quadrupole magnetic tweezers," *IEEE Trans. Robot.*, vol. 26, no. 3, pp. 531–541, Jun. 2010.
- [22] Z. P. Zhang, F. Long, and C. H. Menq, "Three-dimensional visual servo control of a magnetically propelled microscopic bead," *IEEE Trans. Robot.*, vol. 29, no. 2, pp. 373–382, Apr. 2013.
- [23] B. G. Hosu, M. Sun, F. Marga, M. Grandbois, and G. Forgacs, "Eukaryotic membrane tethers revisited using magnetic tweezers," *Phys. Biol.*, vol. 4, no. 2, pp. 67–78, Jun. 2007.
- [24] Z. P. Zhang, Y. H. Shi, S. M. Jhiang, and C. H. Menq, "Mechanical anisotropy and adaptation of metastatic cells probed by magnetic microbeads," in *Proc. Imag., Manipulation, Anal. Biomolecules, Cells, Tissues VIII*, 2010, vol. 7568, pp. 131–137.
- [25] A. H. B. de Vries, B. E. Krenn, R. van Driel, and J. S. Kanger, "Micro magnetic tweezers for nanomanipulation inside live cells," *Biophys. J.*, vol. 88, no. 3, pp. 2137–2144, 2005.
- [26] F. Long, D. Matsura, and C. H. Menq, "Actively controlled hexapole electromagnetic actuating system enabling 3-D force manipulation in aqueous solutions," *IEEE/ASME Trans. Mechatron.*, vol. 21, no. 3, pp. 1540–1551, Jun. 2016.
- [27] F. Long, P. Cheng, T. M. Meng, and C. H. Menq, "Optimal current allocation rendering 3-D magnetic force production in hexapole electromagnetic actuation," *IEEE/ASME Trans. Mechatronics*, vol. 26, no. 5, pp. 2408–2417, Oct. 2021.
- [28] F. Long, T.-M. Meng, J.-J. Wang, and C.-H. Menq, "Hall-sensor-based magnetic force modeling and inverse modeling for hexapole electromagnetic actuation," *IEEE/ASME Trans. Mechatron.*, vol. 27, no. 5, pp. 2806–2817, Oct. 2022.
- [29] T.-M. Meng and C.-H. Menq, "Ultra-precise high-speed untethered manipulation of magnetic scanning microprobe in aqueous solutions," *IEEE/ASME Trans. Mechatron.*, vol. 28, no. 1, pp. 280–291, Feb. 2023, doi: [10.1109/TMECH.2022.3196596](https://doi.org/10.1109/TMECH.2022.3196596).
- [30] W. Coffey, Y. P. Kalmykov, and J. Waldron, *The Langevin Equation: With Applications to Stochastic Problems in Physics, Chemistry and Electrical Engineering*, 2nd ed. Singapore: World Sci., 2004.
- [31] G. F. Franklin, J. D. Powell, and M. Workman, *Digital Control of Dynamic Systems*, 3rd ed. Reading, MA, USA: Addison-Wesley, 1998.
- [32] J. Golten and A. Verwer, *Control System Design and Simulation*. New York, NY, USA: McGraw-Hill, 1991.
- [33] W.-H. Chen, J. Yang, L. Guo, and S. Li, "Disturbance-observer-based control and related methods—An overview," *IEEE Trans. Ind. Electron.*, vol. 63, no. 2, pp. 1083–1095, Feb. 2016.
- [34] M. Tomizuka, "Zero phase error tracking algorithm for digital control," *Amer. Soc. Mech. Eng. J. Dyn. Syst., Meas., Control.*, vol. 109, no. 1, pp. 65–68, Mar. 1987.

- [35] J. Xia and C. H. Menq, "Precision tracking control of non-minimum phase systems with zero phase error," *Int. J. Control.*, vol. 61, no. 4, pp. 791–807, 1995.
- [36] J. Y. Ishihara, M. H. Terra, and J. C. T. Campos, "Robust Kalman filter for descriptor systems," *IEEE Trans. Autom. Control*, vol. 51, no. 8, pp. 1354–1354, Aug. 2006, doi: [10.1109/TAC.2006.878741](https://doi.org/10.1109/TAC.2006.878741).
- [37] P. Cheng, S. M. Jhiang, and C. H. Menq, "Real-time visual sensing system achieving high-speed 3D particle tracking with nanometer resolution," *Appl. Opt.*, vol. 52, no. 31, pp. 7530–7539, Nov. 2013.



Ta-Min Meng received the B.S. degree in power mechanical engineering from the National Tsing Hua University, Hsinchu, Taiwan, in 2015, and the Ph.D. degree in mechanical engineering from The Ohio State University, Columbus, OH, USA, in 2023.

His research interests include modeling, estimation, sensing, and control of precision electromechanical systems.



Chia-Hsiang Menq received the Ph.D. degree in mechanical engineering from Carnegie Mellon University, Pittsburgh, PA, USA, in 1985.

Since 1985, he has been with The Ohio State University, Columbus, OH, USA. Since 2006, he has been the holder of the Ralph W. Kurtz Endowed Chair in Mechanical Engineering with The Ohio State University.

Dr. Menq is a Fellow of the American Society of Mechanical Engineers, the American Association for the Advancement of Science, and the Society of Manufacturing Engineers.